Langevin dynamics/Monte Carlo simulations method for calculating nanoscale dielectric functions of materials

Steven B. Hancock and David P. Landau
Center for Simulational Physics and Department of Physics and Astronomy, University of Georgia, Athens, Georgia 30602, USA

Neda Alsadat Aghamiri and Yohannes Abate*
Department of Physics and Astronomy, University of Georgia, Athens, Georgia 30602, USA

(Received 18 March 2022; accepted 22 June 2022; published 14 July 2022; corrected 16 August 2022)

We have developed a simulational methodology for calculating the nanoscale frequency-dependent complex dielectric function of a wide range of materials using a combination of Langevin dynamics and Metropolis Monte Carlo methods. The premise of such a scheme is to use the atomistic structure of materials and designate appropriate interatomic interactions as well as internal field couplings to accommodate correlated materials. We validate our model by recreating the dielectric functions of well-studied representative materials including insulator SiO_2 thin film that has phonon resonances in the midinfrared, and semiconductor monolayer MoS_2 that exhibits strong excitonic resonances in the visible frequency range. To further showcase the capability of the model in calculating nanoscale dielectric modulation of complex materials, we simulate the dielectric response of $SmNiO_3$, a correlated perovskite oxide, with respect to differing levels of hydrogenation, oxygen vacancy formation, and external fields. This is accomplished by inserting and tracking the movement of dopants at the nanoscale using Metropolis Monte Carlo methods that explicitly include interactions with each other as well as external fields. Simulated nanoscale dielectric spectra agree very well with high-resolution near-field experimental measurements based on scattering type scanning near-field microscopy. We find that this modeling scheme carries a broad utility in describing and predicting the nanoscale dielectric behavior of a broad range of materials exposed to changing local environments.

DOI: 10.1103/PhysRevMaterials.6.076001

I. INTRODUCTION

Simulation of the frequency dependent complex dielectric function $\epsilon(\omega)$ of materials can enable quantitative characterization of experimental spectra and prediction of electronic energy bands, interband transitions, excitons, and plasmons, as well as free carrier and lattice vibrations. Simulational methods become necessary if measured samples have nanoscale inhomogeneities and multilayers that are often difficult to model using simple analytic theories. In view of recent advances in the synthesis of new complex and correlated quantum and nanomaterials, nanoscale simulation of dielectric functions becomes increasingly necessary.

Computational tools have been historically leveraged to recreate the dielectric response of materials at various lengths and time scales. Heisenberg-like models have employed Monte Carlo methods [1] to find relevant electric and magnetic susceptibilities of materials at macroscopic length scales [2,3]. Atomistic models such as TIP3P [4–6] and TIP4P-ϵ [7–9] have been successful in recreating the dielectric function for water and ice. *Ab initio* molecular dynamics simulations as well as density functional theory calculations have been applied to predict the dielectric function of crystalline solids and macromolecules in solution [10–15]. However, it remains a challenge to garner insight into the nanoscale dielectric response of materials under complex nonlocal effects. Therefore, we find it vital to develop an easily implementable and flexible simulational tool for computation of the nanoscale dielectric function that can accommodate varying external conditions that may affect the local nanoscale dielectric properties of quantum and nanomaterials of interest, such as local defects, dopants, external fields, and strain.

In this work we present an intuitive, fast, and versatile atomistic simulational method for calculating the nanoscale dielectric function of materials with relatively simple interatomic potentials. The method uses a combination of Langevin dynamics and Metropolis Monte Carlo simulations. It enables the calculation of nanoscopic modulations in the complex dielectric functions of materials due to defects, vacancy centers, electron-electron correlations, and external stimuli such as strain or fields. We first describe the general formulation of the method and present representative examples of the frequency dependent dielectric function of well-studied materials including the excitonic van der Waals two-dimensional material MoS_2 in the visible frequency range, SiO_2 and locally doped $SmNiO_3$ (SNO) correlated perovskite oxide in the midinfrared frequencies. All simulated spectra agree well with experimentally measured dielectric functions. We compare the simulated modulation of the nanoscale dielectric properties of SNO due to hydrogen

*Corresponding author: yohannes.abate@uga.edu

doping and local oxygen vacancy creation with high-resolution imaging experiments performed using a scattering-type scanning near-field microscope (s-SNOM).

II. MODELS

The polarization **P** of a material due to an applied electric field **E** is $\mathbf{P} = \epsilon_0(\epsilon - 1)\mathbf{E}$, where ϵ is the (frequency dependent) dielectric function and ϵ_0 is the permittivity of free space. We may break up the polarization P into two parts, contributions from dipole moments generated by bound charges, and potential free charges in the material. Thus $\mathbf{P} = \frac{1}{V}(\sum_i \mathbf{p}_i + \sum_j q_{\text{free}}\mathbf{r}_j)$, where V is the volume of the total system, $\mathbf{p}_i$ are the dipole moments potentially generated from distortions of individual unit cells, and the second term accounts for the dipolar contribution of the free charges. The polarization may change over time due to changes in the positions of either the bound or free charges, and enables modeling the time dynamics in a way that is both physically relevant and easily interpretable.

Following the bond charge model [16] particles of positive charge q_I are arranged according to the crystal structure of the material to be modeled. These charged particles represent the lattice ions in the material and they remain mostly stationary, but they may slightly deviate from their ideal lattice positions by amounts that are determined by statistical mechanics and the temperature of the system. We arrange particles of negative charge q_e in between crystal ions to represent electronic charge situated in bonds between parent ions. The ionic degrees of freedom couple to the electronic ones according to a simple harmonic potential given by

$$\mathcal{H}_r = \frac{1}{2}k_r \sum_{i_I, j_e}(r_{i_I, j_e} - r_0)^2 \beta_{i_I, j_e}, \tag{1}$$

where i_I and j_e enumerate the ionic and electronic degrees of freedom, respectively. k_r represents the bond stiffness between the two particles, r_{i_I, j_e} is the instantaneous distance between them, and finally r_0 is the bond's equilibrium length. We employ a so called "bonding index" β_{i_I, j_e} to enforce that we only count harmonic contributions of bonded particles. As such, $\beta_{i_I, j_e} = 1$ if particles i_I, j_e are bonded and 0 otherwise.

Additionally we include a harmonic bond angle interaction to the ionic degrees of freedom to encapsulate more sophisticated dynamics without significantly complicating our existing model. As such, lattice ions indexed with i_I, j_I, k_I, respectively, have a potential given by

$$\mathcal{H}_\theta = \frac{1}{2}k_\theta \sum_{i_I, j_I, k_I}[\cos(\theta_{i_I, j_I, k_I}) - \cos(\theta_0)]^2 \gamma_{i_I, j_I, k_I}, \tag{2}$$

where similarly k_θ is the bond-angle stiffness, θ_{i_I, j_I, k_I} and θ_0 the respective instantaneous and equilibrium angle, and γ_{i_I, j_I, k_I} is analogously a bond angle index defined by $\gamma_{i_I, j_I, k_I} = 1$ if particle i_I shares a bond with particles j_I, k_I, and 0 otherwise.

Therefore, the total Hamiltonian takes the simple form

$$\mathcal{H} = \mathcal{H}_r + \mathcal{H}_\theta. \tag{3}$$

Particle i in a material interacts with a total electric field given by $E_{\text{tot},i} = E_{\text{ext}}(\omega, t) + E_{nn,i} + E_{C,i}$, where $E_{\text{ext}}(\omega, t)$ is a spatially uniform external field driven at angular frequency ω, E_{nn} is the total field generated from screened electric dipole moments from nearest neighbor unit cells, and E_C is the screened Coulomb field from neighboring electrons. E_{nn} and E_C take similar forms:

$$\mathbf{E}_{C,i} = \sum_{j_e} \frac{q_e^2}{4\pi\epsilon r_{ij}} e^{-\alpha r_{ij}}\, \sigma(r_{ij} - \delta)\, \hat{\mathbf{r}}, \tag{4}$$

$$\mathbf{E}_{nn,i} = \sum_{j \in NN} \frac{3(\mathbf{p}_j \cdot n_{ij}) - \mathbf{p}_j}{4\pi\epsilon r_{ij}^3}\, e^{-\beta r_{ij}}, \tag{5}$$

where α, β are phenomenological screening factors, $\mathbf{p}_j$ is the electric dipole moment of the jth nearest neighbor unit cell, n_{ij} is the unit vector pointing from unit cell i to unit cell j, and finally $\sigma(r_{ij} - \delta)$ is the Heaviside-step function to enforce a cutoff radius of length δ.

We make use of Langevin dynamics [4] to describe the force on particle i as

$$\mathbf{F}_i = -\nabla_i \mathcal{H} + Bq_i\mathbf{E}_{\text{tot}} - b_i\mathbf{v}_i + \sqrt{2bk_BT}\mathbf{f}_L, \tag{6}$$

where $-b_i\mathbf{v}_i$ is a phenomenological damping force and $\mathbf{f}_L$ is a force with magnitude distributed about a standard Gaussian and direction uniformly distributed about a sphere. This force is meant to model the deviations in trajectories of particles in the system due to random thermal collisions with the environment. We integrate the above defined equations of motion with the predictor-corrector integration method using time steps in the range of 0.1–10 fs. Typical total integration times were 1–100 ps.

Finally, we include other charged particles that take random trajectories throughout the system to represent the possible contributions of external dopants and/or free charges. We assume that such charges do not interact with the ionic and electronic portions of the lattice and that they only interact with the external electric field as well as each other through a screened Coulomb potential of the form

$$\mathcal{H}_{fd} = \sum_{i,j} \frac{q_d q_f}{4\pi\epsilon r_{ij}} e^{-kr_{ij}}, \tag{7}$$

where the charges of the dopants and free charges are respectively denoted by q_d and q_f. Additionally, i runs over all potential dopants in the system, while j indexes all the free charges. We evaluate the trajectories of the particles using the Metropolis Monte Carlo method [1], where trial moves are generated with random directions and magnitudes uniformly distributed about the interval $[0, r_max]$, where r_max is some maximum hopping distance. These trial moves are then accepted or rejected according to the rule

$$P_{A\to B} = \min\left\{1, \exp\left(-\frac{\Delta_{AB}\mathcal{H}_{fd}}{k_BT}\right)\right\}, \tag{8}$$

with $\Delta_{AB}\mathcal{H}_{fd}$ being the difference in energy between states A and B, respectively, and finally T is the predetermined temperature of the system.

Since $\epsilon(\omega)$ is a complex quantity, we may write

$$\mathbf{P} = s\, e^{i\phi}\mathbf{E} \tag{9}$$

and thus we calculate the dielectric function using the relation

$$\frac{\epsilon}{\epsilon_0} = s[\cos(\phi) + i\sin(\phi)], \tag{10}$$

TABLE I. Summary of numeric values used in the simulations of SiO_2, MoS_2, and SNO. Electrons in different bonds were permitted to have different damping coefficients as illustrated by b_{Sm-e} and b_{Ni-e} for SNO. Ionic degrees of freedom were given the same damping constants $b_{\text{ion}}/m_{\text{ion}} = 1.0\times10^{10}$ (Ns/m) for simplicity since their motions do not contribute significantly to the calculation of $\epsilon(\omega)$ in our simulation.

Material	Damping constants					α (1/m)	β (1/m)	B
SiO_2	b_e/m_e 2.08×10^{14}	b_{Si}/m_{Si} 1.0×10^{10}	b_O/m_O 1.0×10^{10}			9.22×10^{16}	3.84×10^{15}	0.79
MoS_2	b_e/m_e 7.11×10^{16}	b_{Mo}/m_{Mo} 1.0×10^{10}	b_S/m_S 1.0×10^{10}	b_{ex1}/m_e 9.03×10^{10}	b_{ex2}/m_e 9.03×10^{10}	7.56×10^{10}	4.21×10^{10}	0.96
SNO	b_{Sm-e}/m_e 5.61×10^{16}	b_{Ni-e}/m_e 4.19×10^{16}	b_{Sm}/m_{Sm} 1.0×10^{10}	b_{Ni}/m_{Ni} 1.0×10^{10}	b_O/m_O 1.0×10^{10}	2.35×10^{11}	5.81×10^{13}	0.47

where s and ϕ are the amplitude and phase between the polarization and the applied electric field. Therefore, one merely needs to repeat the steps outlined above at different frequencies ω of the external field to reconstruct $\epsilon(\omega)$.

We systematically increase the lattice dimensions $N\times N\times M$ until the change in the dielectric value is less than 5% when compared to systems of size $(N+1)\times(N+1)\times(M+1)$. We utilized $20\times20\times5$ lattices for the SiO_2 and $SmNiO_3$ (SNO) to represent experimental thin films, and $50\times50\times1$ lattices for monolayer MoS_2. All systems utilize periodic boundary conditions in the lateral directions allowing us again to more closely resemble the experimental situation without needing significantly longer computation time. Total computational run time increased approximately quadratically with system size. All error bars provided in the proceeding discussion have been calculated over at least 10 independent runs with different random number strings to randomize initial velocities, noise terms, and free-charge/dopant dynamics.

III. RESULTS

A. Calculated dielectric spectra of SiO_2

As a first example to validate our methods, we use thin film of SiO_2, an insulator oxide used commonly as substrate in experiments and with a well-known dielectric spectra in the midinfrared frequency range. As outlined above, we first assign both bond-length and bond-angle interactions to relevant particles according to the SiO_2 crystal structure. As such, equilibrium bond lengths l_{Si-e} and l_{O-e}, as well as bond angles $\theta_{Si-O-Si}$ and θ_{O-Si-O}, are geometrically predetermined from the crystal structure. Based on the well-known Si-O stretch mode, which is centered at 1075 cm^{-1}, taken from Ref. [17], we assign both $\omega_{0,Si-e} = \omega_{0,O-e} = 1075$ cm^{-1}. We then use the damping factor b, electrostatic parameters α, β, and universal charge scaling factor B as fitting parameters to simulate the experimental data for $\epsilon(\omega)$. Refer to Table I below for a summary of fitting numeric values used in the simulations. We find that the bond-length stiffness $k_{Si-e}$and k_{O-e} impact the overall shape of the spectrum significantly more than the bond angle stiffness $k_{Si-O-Si}$ and k_{O-Si-O}. This is because the associated umbrella modes are much higher in energy than the more simple Si-O stretch modes and thus do not contribute much to this region of the spectrum.

In Fig. 1 we show comparison of our model calculation of the real and imaginary parts of the dielectric function of SiO_2 with experiment [16]. We were able to achieve quantitatively similar results with experimental data, even with a relatively simple model. A source of small discrepancies in the imaginary dielectric spectrum can be attributed to the fact that the simulation uses perfect crystalline SiO_2 with no defects or distortions, which is clearly not the case in the experimental samples used. Such defects will create spectral features that vary between individual samples and will necessarily cause slight variations between the measured and calculated spectra. However, the overall spectral shape garnered with this modeling scheme is strikingly accurate to the experimental data, showing that our atomistic simulational methodology utilizing relatively simple interaction potentials is able to capture the essential features of SiO_2. We note that, while fitting dielectric spectra to a combination of Lorentzian

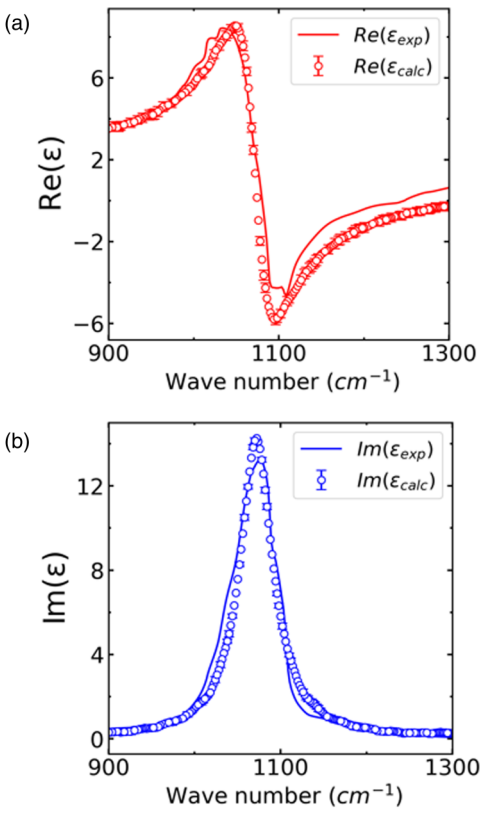

FIG. 1. Comparison between the calculated and experimental results for the dielectric function of SiO_2. The real (a) and imaginary (b) parts of dielectric function for SiO_2; solid lines show experimental data and dotted points are the corresponding calculated results with representative error bars. Where not shown, error bars are smaller than the size of the dotted point.

oscillators may provide agreement with experimental spectra, such a fitting scheme is purely phenomenological and cannot provide insight into the overall atomistic nanoscopic material dynamics. Furthermore, force constants used in recreation of the experimental spectra can be compared with available phonon spectra to provide additional insight into the lattice dynamics of the system.

B. Calculated dielectric spectra of MoS_2

To demonstrate the effectiveness of our model in the visible/near-IR frequency range, we simulate the spectra of a classical transition metal dichalcogenide (TMDC), monolayer MoS_2. Similar to what we described above for SiO_2, we arrange atoms according to the crystal structure of MoS_2 and assign resonances apparent in the experimental spectrum to microscopic force constants available in the simulation. Again, equilibrium bond lengths l_{Mo-e} and l_{S-e}, as well as bond angles $\theta_{Mo-S-Mo}$ and θ_{S-Mo-S}, are predetermined by the crystal structure of the material. As before, we use damping constants b_i, electrostatic parameters α, β, and charge scaling factor B as fitting parameters to approximate the known spectra. Excitonic resonances play a prominent role in MoS_2 [18] and, upon prior knowledge of their existence and associated energy, we may simply model their effect on the spectra by including pairs of opposite charges, coupled together with a harmonic potential with coupling constants k_{ex1}, k_{ex2}, as well as respective damping constants b_{ex1}, b_{ex2}. In Table I below we present a summary of numeric values used in the simulations. We employ Metropolis Monte Carlo methods to update the center of mass position of an individual exciton, each time step, and then we use Langevin dynamics to update the relative positions of the associated charges. In this way we capture both the real-time dynamics as well as the stochastic nature of excitons.

C. Calculated dielectric spectra of $SmNiO_3$

We now demonstrate the use of our model for simulation nanoscale, dynamic changes in carrier density, conductivity, and dielectric spectra of correlated materials. To that end we simulate the dielectric functions and the related features of a prototypical correlated perovskite SNO. Simulation provides insight in atomistic processes as well as the prediction of nanoscale/macroscale properties of this complicated material when exposed to arbitrary external conditions. We investigate the modulation of the dielectric function of SNO when exposed to strong local external fields and the influence of oxygen vacancies caused by such fields. We proceed, as described above, using the atomistic crystal structure of SNO as well as experimental dielectric data to establish relevant bond length and bond angle force constants [19]. As previously mentioned we then use the damping parameters b_i, electrostatic parameters α, β, and charge scaling factor B to fit to the known spectra. As shown in Fig. 3, we were able to recreate the imaginary part of the experimental spectra within error bars. Table I below shows a list of parameters used in the simulation. To further describe the change in spectra of SNO as a result of the effects of interstitial charged dopants, we distribute point charges randomly throughout the system with charges $\pm 1e$,

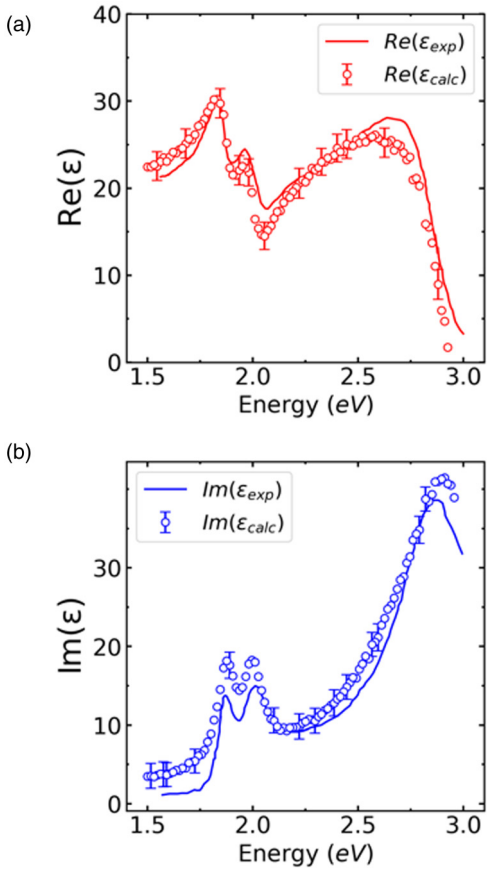

FIG. 2. Comparison between the calculated and experimental results for the dielectric function of MoS_2. The real (a) and imaginary (b) parts of dielectric function for MoS_2; solid lines show experimental data and dotted points are the corresponding calculated results with representative error bars. The error bars in the calculated result are smaller than the dots. We used $50 \times 50 \times 1$ systems with lateral periodic boundary conditions, along with a simple model for the excitonic resonances described in the text.

representing hydrogen ion dopants, and conduction electrons, respectively. These particles interact via a screened Coulomb interaction as described in Eq. (7). Furthermore, their positions are updated at each time step according to the Metropolis criterion [Eq. (8)]. The number of conduction electrons present in the sample is chosen to approximate the charge carrier concentration $n_e \sim \text{Im}[\epsilon(\omega)]$, which for our systems was $N_{\text{free}} \approx 200$. Using this scheme the model predicts the real and imaginary parts of the dielectric spectra in the mid-infrared frequency range that quantitatively agrees with the measurement as shown in Fig. 3 (experimental data taken from Ref [20]). This provides us great confidence that this modeling scheme is able to accurately reproduce the dielectric response of more complex species of correlated materials.

As shown in Figs. 1–3, our simulation protocol predicts satisfactorily the dielectric functions of several prototypical compounds, including SiO_2, TMDCs, and, in particular, monolayer MoS_2 and correlated oxide SNO. We note that the model itself is still a phenomenological description since a couple of fitting parameters exist. Therefore, there is some freedom to adjust the shape of the dielectric function curves

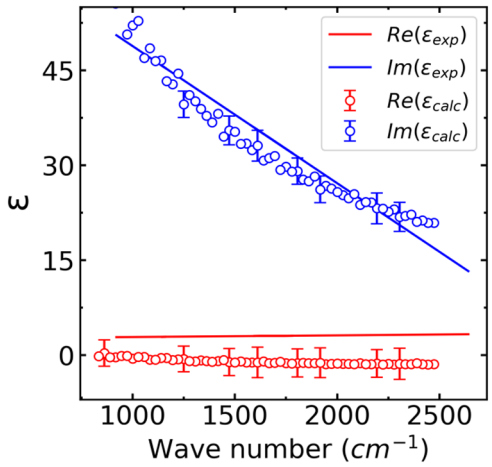

FIG. 3. Comparison between the calculated and experimental results for the dielectric function of SNO. The solid lines show experimental data and dotted points are the corresponding calculated results with representative error bars. We model SNO assigning bond length and bond angle interactions as well as establishing appropriate electrostatic interactions to accommodate electron correlation.

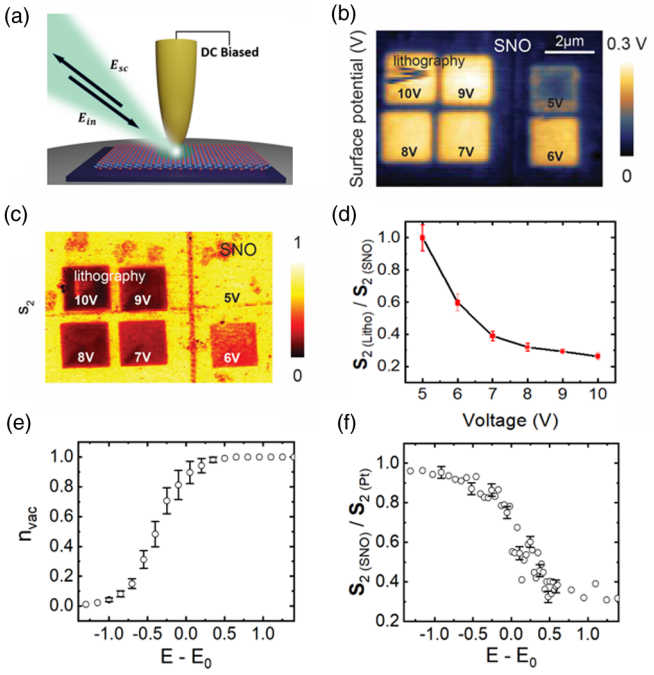

FIG. 4. (a) Schematic of s-SNOM and c-AFM/KPFM experimental setup. (b) Surface potential images of conductive writing patterns onto pristine SNO by applying 5V-10V potential. (c) Corresponding s-SNOM second-harmonic amplitude images taken at 10 μm laser wavelength. (d) Normalized second harmonic amplitude $[s_2(\mathrm{SNO})/s_2(\mathrm{Pt})]$ plots as a function of tip-biasing voltage. (e) The proportion of vacancies created in the simulation as a function of biasing field strength, where 0 indicates no vacancies have been created and 1 meaning that all oxygens have been removed. $E_0 = 5.26\times10^5$(N/C) represents a threshold field strength about which oxygens most actively leave the sample. (f) The calculated normalized amplitude as a function of field strength.

(contributing to the discrepancy between simulations and experimental data shown in Figs. 1, 2, and 3), which is in contrast to what would happen with a model extracted from first principles calculations such as density functional theory. In addition, variation from "perfect" lattices used in the simulation to crystalline imperfections in the experimental samples will further play a role in the minute differences between simulational results and experimental data shown in Figs. 1, 2, and 3. The strength of our empirical model is its ability to provide fast and facile prediction of nanoscale dielectric functions as opposed to time and resource demanding atomistic calculations (e.g., density functional theory and molecular dynamics).

SNO exhibits enormous changes in its dielectric function over a large spectral range by either oxygen vacancy generation or hydrogen doping [21]. Using conductive atomic force microscope (c-AFM) and Kelvin probe force microscope (KPFM) we create nanoscale patterns of various levels of conductivity on SNO and then image their optical contrast using s-SNOM [schematics shown in Fig. 4(a)]. The biased tip generates surface atoms and dissociates them; it also removes oxygen from the SNO surface creating regions of various conductivity regions due to oxygen vacancy generation as shown in Fig. 4(b) [21]. Such local conductivity changes generated by the charge writing process can also be imaged using s-SNOM at spatial resolution only limited by the sharpness of the probe tip (typically 20–50 nm) [22]. The s-SNOM amplitude images shown in Fig. 4(c) were taken at 10 μm laser wavelength and show voltage-dependent s-SNOM optical contrast. The image contrast in s-SNOM represents local conductivity changes [23] of the dark written regions and that a positive bias voltage creates lower conductivity due to the removal of oxygen from the surface of SNO [Figs. 4(b) and 4(c)]. Increasing the tip voltage leads to decreasing the local near-field amplitude (local conductivity) as shown in Fig. 4(d) (see Methods and references therein for more details on the experimental techniques). To model oxygen vacancies and their effect on the nanoscale conductivity of SNO, we assume that oxygen in SNO has a predefined dissociation energy, $E_{\mathrm{Dis},O} = 392$(kJ/mol). We then introduce a static biasing field of varying strength [$E_{\mathrm{Bias}}\ 10^5$ (N/C)] and should the energy of an oxygen atom exceed, $E_{\mathrm{Dis},O}$, it switches to a "vacant state," in that it now interacts with the free charges via a screened Coulomb potential defined above, where the dopant charge $q_d = q_O$, the charge assigned to the oxygen atoms. In this way we track the number of vacancies formed in the system as a function of applied field strength. As the local applied field increases it is able to create additional oxygen vacancies, which decreases the mobility of the simulated free charges and therefore depresses the conductivity. This is shown in Fig. 4(e), where the density of oxygen vacancies, $\rho_{\mathrm{vac}} = n_{\mathrm{vac}}/V$, n_{vac} and V being the number of vacancies and volume of the simulational system, respectively, increases exponentially with increasing field and then reaches a saturation level for a fixed thickness of the sample. We then use the varying vacancy density and simulated the nanoscale dielectric changes due to oxygen vacancies which are directly reflected in the near-field amplitudes s_n [Fig. 4(f)], calculated using the well-known finite dipole model. Similar to the experiment [Fig. 4(d)], the calculated near-field

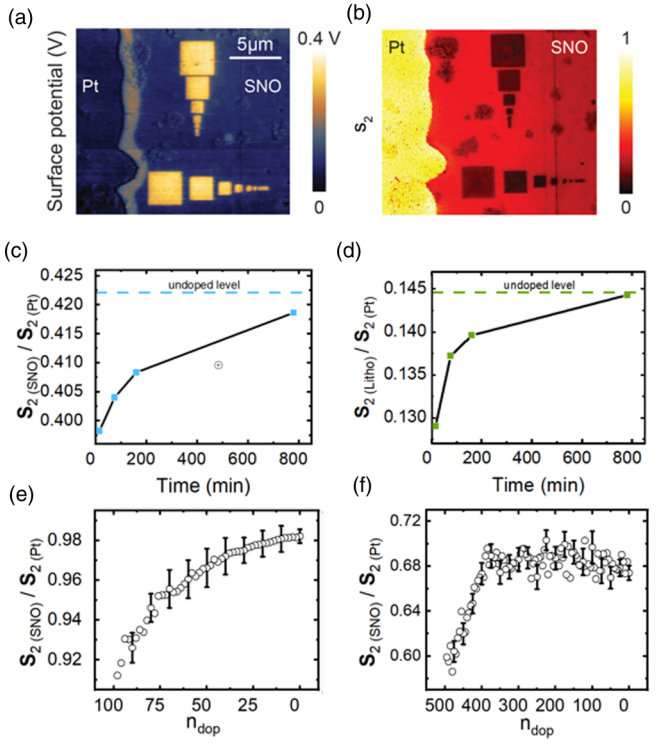

FIG. 5. (a), (b) KPFM surface potential and s-SNOM amplitude images of hydrogen-doped SNO/Pt films, respectively. Normalized amplitude of hydrogen doped pristine SNO (c) and on charge written areas (d). We measure both samples at incremental times from the onset of hydrogenation; as such we see the amplitude slowly return near to its undoped level, indicating a diffusion of hydrogen ions out of the system. Normalized calculated s-SNOM amplitude plot of pristine (e) and oxygen vacant (f) simulated systems, respectively, as a function of the number of hydrogen ions in the system. Calculated results qualitatively reproduce experimental data, being an eventual return to the undoped level as the number of dopants decreases.

amplitude [Fig. 4(f)] starts at a maximum normalized value of one following a logistic trend with increasing field (voltage). This indicates a route to tuning the conductivity/dielectric properties of the sample via varying the strength of the applied field.

Incorporation of hydrogen dopants is a robust way to modify the dielectric properties of SNO [24]. The pristine and charge written areas of SNO were exposed to H_2 (written patterns were produced deliberately close to the Pt electrode to initiate hydrogen catalysis) and imaged using s-SNOM at 10 μm laser wavelength [Figs. 5(a) and 5(b)]. Multiple s-SNOM images were taken as a function of time and normalized second harmonic amplitude signals [s_2(SNO)/s_2(Pt)] were extracted and plotted for the pristine [Fig. 5(c)] and charge written [Fig. 5(d)] areas. Hydrogen diffuses out from the sample with time in both the pristine and charge written areas as the sample recovers to the undoped values 800 min after the initial arbitrarily doped state as shown in Figs. 5(c) and 5(d). To simulate this effect of the hydrogenation process, we initialize SNO as described above, randomly distributing dopants and conduction electrons throughout the sample that interact with each other via H_{fd} [Eq. (7)]. The simulated normalized amplitude for pristine and oxygen vacant systems qualitatively agree with the experimental trend [Figs. 5(e) and 5(f)] [21]. Since the free charges do not couple to anything other than the dopants we can interpret our results as the dopants localizing the free charges, inhibiting them from contributing to the amplitude as they would have without doping. An increase in hydrogen dopant density ($\rho_{\text{dop}} = n_{\text{dop}}/V$) in the simulation (which corresponds to increasing time after the initial doping) is accompanied by a decrease in the normalized amplitude signal and the saturation limit is the initial undoped state of the sample. In this way the simulation provides qualitative dependence between dopant/oxygen vacancy density and conductivity changes (s-SNOM contrast) as shown in Figs. 5(e) and 5(f).

IV. CONCLUSIONS

The array of nanoscale dielectric function and conductivity results presented in this work emphatically demonstrate the use of the modeling scheme we present. We have not only been able to quantitatively recreate known experimental dielectric data, but also provided a framework that allows for relative ease of interpretation of such spectra. Furthermore, we are able to provide quantitative insight into nanoscale dielectric modulation of SNO due to external manipulation (hydrogen doping and local oxygen vacancy formation). Our simulational procedure provides a method by which one may garner both intuitive and quantitative understanding of the complex nansocale dielectric behavior of materials without having to resort to more resource intensive computational means.

V. EXPERIMENTAL METHODS

The Cypher atomic force microscope (AFM) (Oxford Instruments) is used to perform conductive AFM (c-AFM) as well as the scanning Kelvin probe microscope (SKPM). The lithography patterns were made by c-AFM; a contacted mode AFM was performed while applying voltage through the metal Ti/Ir coated tip (Asyelectric.01-R2 from Oxford). SKPM is then used to measure the surface potential of the written structures [Figs. 4(b) and 5(a)]. A scattering type scanning near-field microscope (s-SNOM) is used to acquire topography and near-field images of the SNO sample prepared by PVD on $LaAlO_3$ substrates. s-SNOM [Fig. 4(a), neaspec co.] is based on a tapping mode AFM with a cantilevered metal-coated tip that oscillates at a resonance frequency, $W \sim 280$ kHz, and tapping amplitude of ~50 nm. A focused infrared laser beam on the metalized tip interacts with the sample, and the scattered light from this interaction is demodulated at higher harmonics nΩ of the tapping frequency and detected via phase modulation interferometer. s-SNOM enables mapping the dielectric function of materials at the nanoscale in a wide spectral range from visible to terahertz frequencies [23,25,26].

ACKNOWLEDGMENTS

This work was supported by the Air Force Office of Scientific Research (AFOSR), Grant No. FA9559-16-1-0172, and National Science Foundation (NSF), Grant No. DMR-1904097. The authors acknowledge Zhen Zhang and

Shriram Ramanathan (School of Materials Engineering, Purdue University) for fabricating and providing all the perovskite nickelate films utilized in this study, as well as for technical discussions relating to the c-AFM measurements.

[1] D. P. Landau and K. Binder, *A Guide to Monte Carlo Simulations in Statistical Physics*, 5th ed. (Cambridge University Press, Cambridge, UK, 2021).

[2] J. A. Barker and R. O. Watts, Monte Carlo studies of the dielectric properties of water-like models, Mol. Phys. **26**, 789 (1973).

[3] Z. Fadil, A. Mhirech, B. Kabouchi, L. Bahmad, and W. Ousi Benomar, Dielectric properties of a monolayer nano-graphyne structure: Monte Carlo simulations, Superlattices Microstruct. **135**, 106285 (2019).

[4] W. L. Jorgensen, J. Chandrasekhar, J. D. Madura, R. W. Impey, and M. L. Klein, Comparison of simple potential functions for simulating liquid water, J. Chem. Phys. **79**, 926 (1983).

[5] D. Braun, S. Boresch, and O. Steinhauser, Transport and dielectric properties of water and the influence of coarse-graining: comparing BMW, SPC/E, and TIP3P models, J. Chem. Phys. **140**, 064107 (2014).

[6] P. Höchtl, S. Boresch, W. Bitomsky, and O. Steinhauser, Rationalization of the dielectric properties of common three-site water models in terms of their force field parameters, J. Chem. Phys. **109**, 4927 (1998).

[7] R. Fuentes-Azcatl and J. Alejandre, Non-polarizable force field of water based on the dielectric constant: TIP4P/ϵ, J. Phys. Chem. B **118**, 1263 (2014).

[8] A. Ghoufi, A. Szymczyk, R. Renou, and M. Ding, Calculation of local dielectric permittivity of confined liquids from spatial dipolar correlations, EPL (Europhys. Lett.) **99**, 37008 (2012).

[9] E. Meneses-Juárez, J. F. Rivas-Silva, and M. González-Melchor, Static dielectric constant of water within a bilayer using recent water models: a molecular dynamics study, J. Phys.: Condens. Matter **30**, 195001 (2018).

[10] J. L. Fattebert and F. Gygi, Density functional theory for efficient *ab initio* molecular dynamics simulations in solution, J. Comput. Chem. **23**, 662 (2002).

[11] N. Karasawa and W. A. Goddard III, Dielectric-properties of poly(vinylidene fluoride) from molecular-dynamics simulations, Macromolecules **28**, 6765 (1995).

[12] A. Mattoni and C. Caddeo, Dielectric function of hybrid perovskites at finite temperature investigated by classical molecular dynamics, J. Chem. Phys. **152**, 104705 (2020).

[13] T. Simonson and C. L. Brooks, Charge screening and the dielectric constant of proteins: Insights from molecular dynamics, J. Am. Chem. Soc. **118**, 8452 (1996).

[14] J. Y. Yang, L. H. Liu, and J. Y. Tan, First-principles molecular dynamics study on temperature-dependent dielectric function of bulk 3C and 6H SiC in the energy range 3–8 eV, Phys. B: Condens. Matter **436**, 182 (2014).

[15] M. A. Young, B. Jayaram, and D. L. Beveridge, Local dielectric environment of B-DNA in solution: Results from a 14 ns molecular dynamics trajectory, J. Phys. Chem. B **102**, 7666 (1998).

[16] R. Martin, A simple bond charge model for vibrations in covalent crystals, Chem. Phys. Lett. **2**, 268 (1968).

[17] L. M. Zhang, G. O. Andreev, Z. Fei, A. S. McLeod, G. Dominguez, M. Thiemens, A. H. Castro-Neto, D. N. Basov, and M. M. Fogler, Near-field spectroscopy of silicon dioxide thin films, Phys. Rev. B **85**, 075419 (2012).

[18] Y. Li, A. Chernikov, X. Zhang, A. Rigosi, H. M. Hill, A. M. van der Zande, D. A. Chenet, E.-M. Shih, J. Hone, and T. F. Heinz, Measurement of the optical dielectric function of monolayer transition-metal dichalcogenides: MoS_2, $MoSe_2$, WS_2, and WSe_2, Phys. Rev. B **90**, 205422 (2014).

[19] A. Jain, S. P. Ong, G. Hautier, W. Chen, W. D. Richards, S. Dacek, S. Cholia, D. Gunter, D. Skinner, G. Ceder, and K. A. Persson, Commentary: The materials project: A materials genome approach to accelerating materials innovation, APL Mater. **1**, 011002 (2013).

[20] Z. Li, Y. Zhou, H. Qi, Q. Pan, Z. Zhang, N. N. Shi, M. Lu, A. Stein, C. Y. Li, S. Ramanathan, and N. Yu, Correlated perovskites as a new platform for super-broadband-tunable photonics, Adv. Mater. **28**, 9117 (2016).

[21] M. Kotiuga, Z. Zhang, J. Li, F. Rodolakis, H. Zhou, R. Sutarto, F. He, Q. Wang, Y. Sun, Y. Wang, N. A. Aghamiri, S. B. Hancock, L. P. Rokhinson, D. P. Landau, Y. Abate, J. W. Freeland, R. Comin, S. Ramanathan, and K. M. Rabe, Carrier localization in perovskite nickelates from oxygen vacancies, Proc. Natl. Acad. Sci. USA **116**, 21992 (2019).

[22] V. E. Babicheva, S. Gamage, M. I. Stockman, and Y. Abate, Near-field edge fringes at sharp material boundaries, Opt. Express **25**, 23935 (2017).

[23] Y. Abate, D. Seidlitz, A. Fali, S. Gamage, V. Babicheva, V. S. Yakovlev, M. I. Stockman, R. Collazo, D. Alden, and N. Dietz, Nanoscopy of phase separation in $In_xGa_{1-x}N$ alloys, ACS Appl. Mater. Interfaces **8**, 23160 (2016).

[24] Y. Zhou, X. F. Guan, H. Zhou, K. Ramadoss, S. Adam, H. J. Liu, S. Lee, J. Shi, M. Tsuchiya, D. D. Fong, and S. Ramanathan, Strongly correlated perovskite fuel cells, Nature (London) **534**, 231 (2016).

[25] Y. Ogawa, F. Minami, Y. Abate, and S. R. Leone, Nanometer-scale dielectric constant of Ge quantum dots using apertureless near-field scanning optical microscopy, Appl. Phys. Lett. **96**, 063107 (2010).

[26] R. Jing, Y. Shao, Z. Fei, C. F. B. Lo, R. A. Vitalone, F. L. Ruta, J. Staunton, W. J. Zheng, A. S. McLeod, Z. Sun, B. Y. Jiang, X. Chen, M. M. Fogler, A. J. Millis, M. Liu, D. H. Cobden, X. Xu, and D. N. Basov, Terahertz response of monolayer and few-layer WTe_2 at the nanoscale, Nat. Commun. **12**, 5594 (2021).

Correction: The omission of an acknowledgment statement has been fixed.